Magnetohydrodynamics of laser-produced high-energy-density plasma in a strong external magnetic field

Kazuki Matsuo,[1] Hideo Nagatomo,[1] Zhe Zhang,[1] Philippe Nicolai,[2] Takayoshi Sano,[1] Shohei Sakata,[1] Sadaoki Kojima,[1] Seung Ho Lee,[1] King Fai Farley Law,[1] Yasunobu Arikawa,[1] Youichi Sakawa,[1] Taichi Morita,[3] Yasuhiro Kuramitsu,[4] Shinsuke Fujioka,[1,*] and Hiroshi Azechi[1]

[1]*Institute of Laser Engineering, Osaka University, 2-6 Yamada-oka, Suita Osaka, 565-0871, Japan*

[2]*CELIA, University of Bordeaux, 351 Cours de la Liberation, 33405 Talence, France*

[3]*Interdisciplinary Graduate School of Engineering Science, Kyushu University, 6-1 Kasuga-kouen, Kasuga, Fukuoka 816-8580, Japan*

[4]*Department of Physics, National Central University, No. 300, Jhongda Road, Jhongli, Taoyuan 320, Taiwan*

(Received 12 September 2016; published 9 May 2017)

Recent progress in the generation in the laboratory of a strong (>100-T) magnetic field enables us to investigate experimentally unexplored magnetohydrodynamics phenomena of a high-energy-density plasma, which an external magnetic field of 200–300 T notably affects due to anisotropic thermal conduction, even when the magnetic field pressure is much lower than the plasma pressure. The external magnetic field reduces electron thermal conduction across the external magnetic field lines because the Larmor radius of the thermal electrons in the external magnetic field is much shorter than the mean free path of the thermal electrons. The velocity of a thin polystyrene foil driven by intense laser beams in the strong external magnetic field is faster than that in the absence of the external magnetic field. Growth of sinusoidal corrugation imposed initially on the laser-driven polystyrene surface is enhanced by the external magnetic field because the plasma pressure distribution becomes nonuniform due to the external magnetic-field structure modulated by the perturbed plasma flow ablated from the corrugated surface.

DOI: 10.1103/PhysRevE.95.053204

I. INTRODUCTION

The magnetohydrodynamics (MHD) of a high-energy-density plasma (HEDP) in an external magnetic field involve fundamental physics relevant to the fields of astronomy and solar physics [1–11] and to inertial confinement fusion [12–20]. Especially in the magnetic-field-assisted fast ignition scheme, Strozzi *et al.* demonstrated guiding of relativistic electrons generated by intense laser-plasma interactions with a kilotesla magnetic field using two-dimensional hybrid simulation [14]. Laser-driven implosion under a magnetic field of several hundreds of teslas is necessary to apply this guiding scheme to an actual fast ignition experiment. Nagatomo *et al.* found in a simulation significant perturbation growth of an imploding shell under a 100-T external magnetic field [16].

Hydrodynamics under an external magnetic field have been reported in the field of astrophysics. For example, Stone *et al.* studied nonlinear evolution of the magnetic Rayleigh-Taylor instability using three-dimensional magnetohydrodynamic simulations. They found that the restitution force of the external magnetic field reduces the shear flow at a fluid boundary, and this results in reducing fluid mixing [5]. Chambers *et al.* found solutions of the growth of magnetic Rayleigh-Taylor instability in a cylindrical geometry [6].

Although there are several numerical studies in this research area, few fundamental experiments have been performed, mainly due to the lack of a strong magnetic-field source. Recent significant progress in the generation in the laboratory of a strong (>100-T) magnetic field enables us to investigate experimentally unexplored MHD phenomena of an HEDP.

II. TRAJECTORY OF LASER-DRIVEN HEDP UNDER A STRONG MAGNETIC FIELD

A basic experiment in a simple geometry can be performed with a spatially uniform strong magnetic field generated by using a pair of laser-driven capacitor coil targets [21–28]. For simplicity, the experiments were performed with a planar target in two magnetic-field geometries: $B_{\parallel}$ and $B_{\perp}$ are external magnetic fields with directions parallel and perpendicular to the plasma motion, respectively, as shown in Figs. 1(a) and 1(b). In a capacitor-coil target, two nickel disks are connected by a 900-μm-diameter nickel coil. The first nickel disk is irradiated through the hole in the second nickel disk by a GEKKO-XII laser of 1.5 ± 0.1 kJ, with a Gaussian shape with 1.2-ns full width at half-maximum (FWHM) and an intensity of around 1.5×10^{15} W/cm^2. A plasma is generated at the first disk, and suprathermal hot electrons with temperatures exceeding 10 keV are generated in the plasma corona. The hot electrons move ahead of the expanding plasma plume and are accumulated on the second disk. The second disk acquires negative charges, and a large electrical potential develops between the disks. That potential difference drives a current in the coil. A strong magnetic-field pulse is generated in the coil, and the coils are destroyed after every laser shot.

The magnetic flux density was characterized using a three-axis B-dot probe [29] and Faraday rotation with a terbium gallium garnet (TGG) crystal as the magneto-optical material. The B-dot probe and TGG crystal were placed 70 and 4 mm away from the coil center, respectively. The Faraday rotator (a piece of TGG) makes significant noise in the B-dot probe signal; we did not use simultaneously both Faraday rotation and a B-dot probe in the shots. The mechanism of the noise generation is not understood. The magnetic flux densities were

*sfujioka@ile.osaka-u.ac.jp

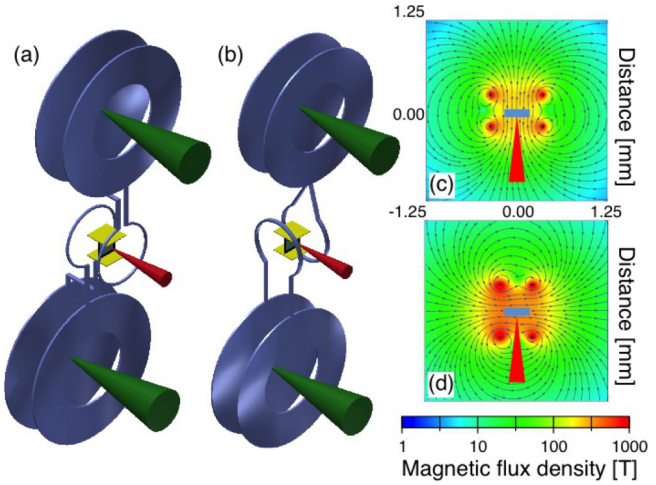

FIG. 1. Experimental configurations for studying the hydrodynamics of HEDPs in an external magnetic field. (a) Experimental setup for the $B_\parallel$ geometry, in which the magnetic-field lines are parallel to the ablated plasma motion. (b) Experimental setup for the $B_\perp$ geometry, in which the magnetic-field lines are perpendicular to the ablated plasma motion. Tantrum plates, 50 μm thick, are placed at the bottom and top of the polystyrene foils to prevent the foils from being preheated by x rays generated at the capacitor plates. Magnetic-field structures computed using the RADIA code for the (c) $B_\parallel$ and (d) $B_\perp$ geometries.

reconstructed using the RADIA code [30] to evaluate the current inside the coil and the magnetic-field structure around the target position, as shown in Figs. 1(c) and 1(d). The results are summarized in Table I.

The average flux densities of $B_\parallel$ and $B_\perp$ at the midpoint between the coils were 215 ± 21 and 350 ± 19 T, respectively. The errors in the B-field measurement mainly came from build variations in the coils. Build variations affect the laser spot size and beam focused on the first disk. The difference between the $B_\parallel$ and the $B_\perp$ strengths may have been due to the difference in the coil inductance and resistance. It is necessary to change coil shapes to produce $B_\parallel$ and $B_\perp$ geometries because all laser beams come from one direction at our laser facility. As a result of the difference in the coil shape, the inductance and resistance of the $B_\perp$ geometry coil are 1.33 and 0.87 times those of the $B_\parallel$ one. The differences in inductance and resistance correspond to $B_\parallel/B_\perp = 1.33$ calculated with a simple circuit model; this is not inconsistent with the experimental value ($B_\parallel/B_\perp = 1.63 \pm 0.18$), however, there may be other, unrecognized differences.

Figures 2(a) and 2(b) show top and face views of the target used in the trajectory measurement. A 25-μm-thick polystyrene (C_8H_8) foil was irradiated with laser beams midway between the two coils. The width of the polystyrene foil along the line of sight of the diagnostics was 150 μm. Fifty-micrometer tantrum plates are placed at the bottom and top of the polystyrene foil as shown in Figs. 1(a) and 1(b) to prevent the polystyrene foil from being preheated by x rays generated at the capacitor parts. Three 351-nm beams of the GEKKO-XII laser were used to drive the foil at an intensity of $4.0 \pm 0.1 \times 10^{13}$ W/cm^2. The magnetic-field strength reaches its peak 1.5 ns after the peak of the magnetic-field-generation laser pulse; this is the same as the result in Ref. [24]. The external magnetic field must diffuse into the polystyrene foil before foil acceleration, therefore the drive laser beams were delayed by 1.5 ns with respect to the magnetic-field-generation beams. Figures 2(c)–2(e) show shadows of the laser-driven polystyrene foils that were observed using an x-ray streak camera and side-on backlighting. The backlight was 1.2-keV x rays emitted due to M shell–to–L shell transitions of bounded electrons of Cu ions in a laser-produced Cu plasma. The pulse duration of the backlit x rays was 1.2 ns. The spatial and temporal resolutions of the x-ray imaging system were measured to be 13 μm and 40 ps, respectively. The flying velocities of the rear surfaces accelerated in the $B_\parallel$ and $B_\perp$ fields are 1.5 times faster than in the absence of an external magnetic field as shown in Figs. 2(f)–2(h). This acceleration mechanism is discussed below.

The magnetic field generated by the Biermann battery effect [31–34] is estimated to be 10 T in this experiment. The self-generated-field contribution is relatively small compared to the external magnetic field. Only the external magnetic field is considered in the following discussion.

The direct effect of the magnetic field on the plasma hydrodynamics is evaluated with the dimensionless parameter $\beta = P_{\rm plasma}/P_{\rm mag}$, i.e., the ratio between the plasma pressure ($P_{\rm plasma}$) and the magnetic field pressure ($P_{\rm mag} = B^2/8\pi$). The β value is evaluated to be about 50 with typical plasma parameters in this experiment. The contribution of the magnetic-field pressure to the plasma acceleration is negligibly small.

The other important parameter is the Hall parameter $\chi = \omega_{\rm ce}\tau_{\rm e}$, where $\omega_{\rm ce}$ and $\tau_{\rm e}$ are the electron gyrofrequency and electron collision time, respectively. For a 300-eV polystyrene plasma and a 200-T external magnetic field, the Hall parameter is close to unity. When the Hall parameter is nonzero, the external magnetic field reduces electron thermal conduction across the external magnetic-field lines because the Larmor radius of

TABLE I. Summary of the magnetic flux density and current in the coil.

Shot ID No.	Geometry	E_L (J)	I_L (W/cm^2)	B at measure (T)	B at center (T)	I_c (kA)	Diagnostics
38043	$B_\parallel$	1263	1.49×10^{15}	1.4	206	210	Faraday
38047	$B_\perp$	1267	1.49×10^{15}	0.00407	349	295	B-dot
38051	$B_\parallel$	1266	1.49×10^{15}	0.00417	239	244	B-dot
38054	$B_\parallel$	1306	1.54×10^{15}	0.00350	201	205	B-dot
38055	$B_\perp$	1316	1.55×10^{15}	0.0388	332	281	B-dot
38056	$B_\perp$	1308	1.54×10^{15}	0.00430	369	312	B-dot

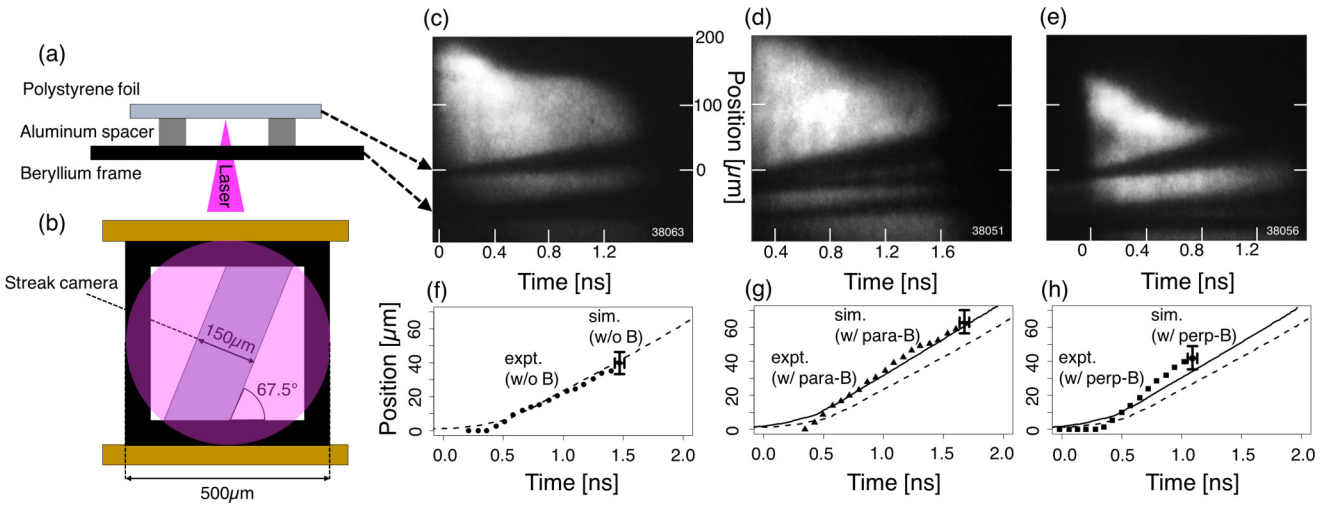

FIG. 2. (a) Top view of the target used in a trajectory measurement. A 25-μm-thick polystyrene foil was mounted on a 25-μm-thick beryllium frame. A 50-μm-thick aluminum spacer was inserted between the foil and the frame. (b) Face view of a target used in the trajectory measurement. The width of the polystyrene foil was 150 μm along the line of sight of the diagnostics. The polystyrene foil and the beryllium frame are irradiated by the 500-μm diameter laser beam. Shadow of laser-driven polystyrene foils measured using side-on x-ray backlighting (c) with no external magnetic field and (d) in the $B_\parallel$ and (e) $B_\perp$ geometries. The rear surfaces of laser-driven polystyrene foils (black symbols) are compared with the results of simulations carried out using the PINOCO-MHD code for (f) no external magnetic field and for (g) the $B_\parallel$ and (h) the $B_\perp$ geometries. Solid black and dashed lines are PINOCO-MHD calculations with and without consideration of the external magnetic field, respectively. The origins of the axes are defined as the laser peak timing and initial position of the target's rear surface.

the thermal electrons in the external magnetic field is much shorter than the mean free path of the thermal electrons. The electron temperature increment is modified by the magnetic field through the anisotropic thermal conductivity.

The magnetic Reynolds number $\mathrm{Re}_m = \tau_{\mathrm{diffusion}}/\tau_{\mathrm{hydrodynamics}}$ is the ratio of the magnetic-field diffusion time ($\tau_{\mathrm{diffusion}}$) to the hydrodynamic time scale ($\tau_{\mathrm{hydrodynamics}}$). This dimensionless parameter is important for understanding the dynamics of the magnetic field associated with plasma motion. $\tau_{\mathrm{diffusion}} = 4\pi\sigma L^2/c^2$, where σ is the conductivity of the plasma and L is the typical plasma scale. For example, in a 300-eV polystyrene plasma, $\tau_{\mathrm{diffusion}} > 10$ ns, and the hydrodynamic time scale is $L/C_s \sim 100\ \mu\mathrm{m}/10^7\ \mathrm{cm/s} = 1$ ns, where C_s is the sound velocity of the plasma. Re_m is about 10 for this plasma. Therefore, magnetic-field fluxes are frozen in the plasma, and the field structure changes with the plasma motion. The external magnetic field moves with the plasma flow owing to its large Re_m.

We performed two-dimensional radiation-hydrodynamic simulations (PINOCO-MHD) with and without an external magnetic field. The models used in the PINOCO-MHD code are described in Refs. [16] and [19]. The thermal conductivity becomes anisotropic in both the $\mathrm{B}_\parallel$ and the $\mathrm{B}_\perp$ cases in the simulation. Because anisotropic thermal diffusion reduces the thermal energy loss from the ablated plasma to its cold peripheral region that is transverse to the $B_\parallel$-field lines, the temperature and pressure of the ablated plasma increase significantly, resulting in acceleration of the polystyrene foil by the larger pressure gradient [Figs. 3(a), 3(c), and 3(e)].

The situation is more complex for the $B_\perp$ geometry than for the $B_\parallel$ geometry. There is shear flow in the ablated plasma that is perpendicular to the $B_\perp$-field lines, because ablated plasma flow directed along the target normal within the laser spot region is faster than that in its cold periphery. The $B_\perp$ lines are bent and a $B_\parallel$ component appears at the edge of the target. Thermal energy loss from the ablated plasma to its cold peripheral region is reduced in this magnetic-field structure, the temperature and pressure of the ablated plasma increase significantly, resulting in acceleration of the polystyrene foil by the larger pressure gradient [Figs. 3(b), 3(d), and 3(f)].

In the $B_\perp$ geometry, the measured trajectory is faster than the calculated one. This different may be caused by the Nernst effect. The Nernst effect causes convective amplification of the magnetic field in a laser-produced plasmas near the ablation surface [35]. The Nernst effect cannot be taken into account in the PINOCO-MHD, because this effect is three-dimensional. The present PINOCO-MHD simulation does not explain completely the experimental results obtained in the $B_\perp$ cases because of the Nernst effect. In the $B_\parallel$ geometry, the direction of the electrons that move from the high-temperature to the low-temperature side and the direction of the external magnetic field are parallel. Therefore the Nernst effect is not effective in the $B_\parallel$ geometry.

III. HYDRODYNAMIC INSTABILITY OF LASER-DRIVEN HEDP UNDER A STRONG MAGNETIC FIELD

The hydrodynamic perturbation growth is also affected by the external magnetic field as a result of the anisotropic thermal conductivity in the ablated plasma. A 50-μm wavelength sinusoidal perturbation with initial amplitude $a_0 = 1.6$ or 3.2 μm was imposed on planar polystyrene foils, whose initial thickness $l_0 = 16$ or 25 μm. Two capacitor-coil targets were arranged in the $B_\parallel$ geometry, and the corrugated polystyrene foil was located at the midpoint between the two coils. Face-on x-ray backlighting coupled with an x-ray streak camera was used to measure the temporal evolution of the areal density modulations ($\Delta\rho a$) amplified by the hydrodynamic instability

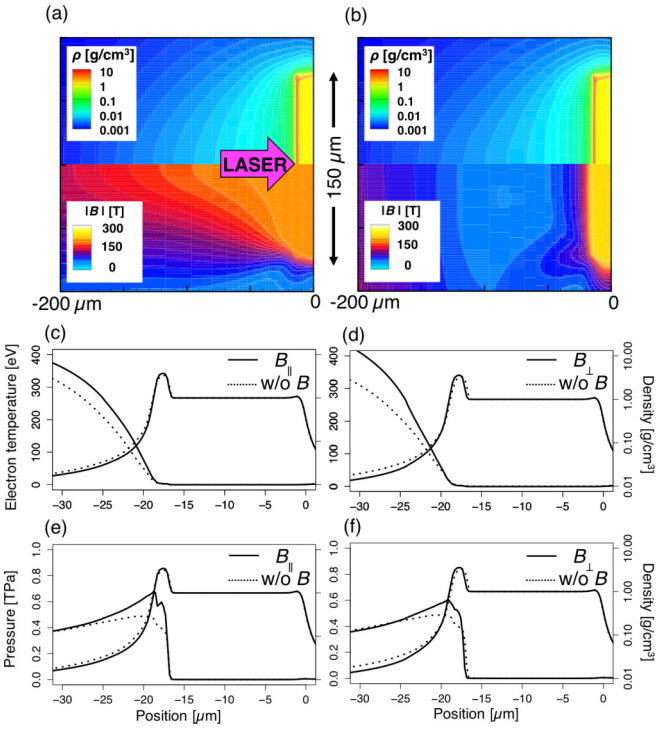

FIG. 3. Two-dimensional mass density and magnetic flux density distributions at the laser peak timing for (a) $B_\parallel$ and (b) $B_\perp$. The origin of the position is defined as the initial position of the target's rear surface. (c–f) Electron temperature and pressure profiles along the target's center axis The electron temperature (solid lines) of the ablated plasmas increases notably in the external magnetic field due to anisotropic thermal conduction as shown for $B_\parallel$ (c) and $B_\perp$ (d) compared to that without a magnetic field (dotted lines). The pressure (solid lines) of the ablated plasmas also increases in the external magnetic field, as shown for $B_\parallel$ (e) and $B_\perp$ (f) compared to that without a magnetic field (dotted lines).

from the x-ray intensity ratio between the peak ($I_{\rm peak}$) and the valley ($I_{\rm valley}$) of an image as $\Delta\rho a = \ln(I_{\rm peak}/I_{\rm valley})/2\mu$, where $\mu = 607\ {\rm g/cm^2}$ is the mass absorption rate of a polystyrene for the x rays. Laser-produced Zn plasmas were used as the x-ray backlighting sources, which emit relatively broad L-shell x rays centered at 1.5 keV. A 5.5-μm-thick Al foil (K absorption edge at 1.56 keV) and a 25-μm-thick Be foil were placed in front of the x-ray streak camera for x-ray filtering. We did not perform this experiment using the $B_\perp$ geometry due to a shortage of experimental time.

The magnetic-field lines move together with the ablated plasma due to its large Re_m. The direction of the ablated plasma flow is normal to the target surface, and ablated plasma accumulates at the valley of the sinusoidal perturbation. Therefore, the external magnetic field is compressed (decompressed) at the valley (peak) of the sinusoidal perturbation [Fig. 4(c)]. The thermal conductivity across the magnetic-field lines is reduced at the valley compared to that at the peak [Fig. 4(b)]. The temperature increases at the valley due to the anisotropic thermal conduction in the perturbed magnetic-field structure as shown in Figs. 4(a) and 4(b). The pressure distribution becomes spatially nonuniform and leads to enhancement of the perturbation growth.

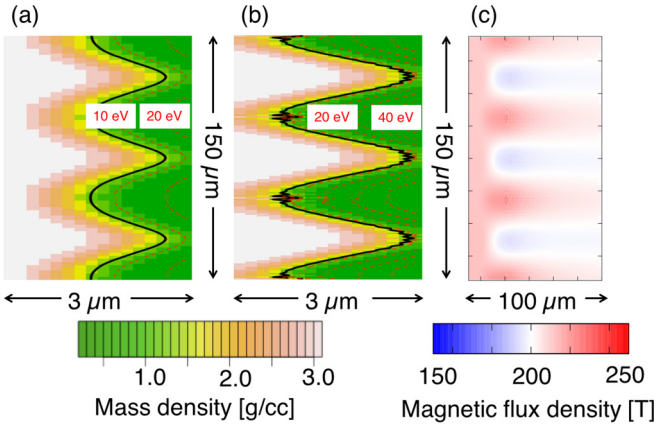

FIG. 4. Snapshot of 50-μm-wavelength perturbations on a laser-accelerated polystyrene foil simulated using the PINOCO-MHD code for (a) no external magnetic field and (b) the $B_\parallel$ geometry. Solid black lines are lines of equal density for the target solid density of 1 g/cm^3, and dashed red lines are isotherms of the electron temperature plotted in 10-eV increments. (c) The anisotropic thermal conduction in the perturbed magnetic-field structure leads to enhancement of the perturbation growth.

The PINOCO-MHD code was used to reproduce the temporal evolution of the experimentally observed perturbation growth. In our previous studies [36,37], growth of a 50-μm perturbation was found to be significantly slow compared to the simulation and theoretical predictions. Similar results were obtained also in the other facilities' experiments [38–40]. We artificially reduced the laser intensity by $\times 0.25$ to fit the computed growth to the experimental ones for the case of no external magnetic field, and the same reduction factor was used to compute the perturbation growth for the $B_\parallel$ geometry. The spatial and temporal resolutions of the imaging system were 13 μm and 150 ps, respectively. The modulation transfer function (MTF) of the imaging system was measured in separate shots, and the MTF was used to obtain the actual amplitude of the areal density modulations from the measured one as shown in Fig. 5(a). The PINOCO-MHD code reproduces

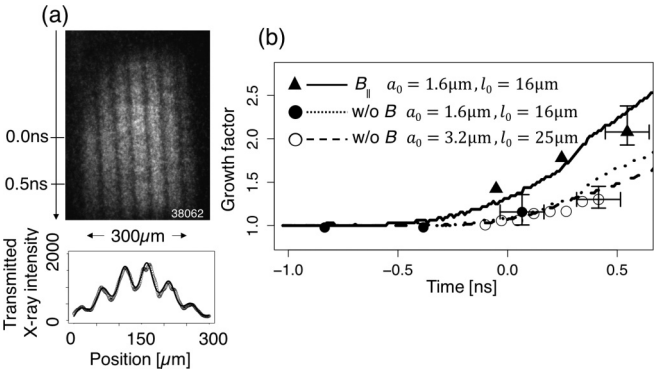

FIG. 5. (a) Face-on x-ray backlight image and its line-out at the laser peak timing. The origin of the axis is defined as the laser peak timing. (b) Comparison of the temporal evolution of areal density modulations measured in the experiment versus calculated by the PINOCO-MHD code.

the experimental trend with the reduced laser intensity, as shown in Fig. 5(b).

Hydrodynamic instability growth is reduced by the restitution force of the magnetic field bent by nonniform plasma flow in a low-β plasma and the external magnetic field having the critical strength [5,8]. In our high-β plasma, the restitution force of the magnetic field to hydrodynamics instability growth is negligibly low. And also, an ablated plasma flow across the fluid boundary plays an essential role in the ablative hydrodynamic instability. The previous analysis, in which ablation effects are neglected, cannot be directly applied to our result.

Instability growth in the $B_\perp$ geometry is also simulated for a reference. An ablated plasma flow carries away the external magnetic field from the laser absorption region, therefore, the hydrodynamics growth is not affected by the $B_\perp$ magnetic field in this simulation.

IV. CONCLUSION

We have demonstrated experimentally that a 200- to 300-T external magnetic field noticeably affects the hydrodynamics and instability growth of an HEDP, even for high-β plasmas. This experimental result suggests that the magnetic field seeds nonspherical symmetrical structures in an HEDP by anisotropic thermal conduction. These effects must be considered in the design of magnetically assisted inertial confinement fusion, which may be an alternative to fusion ignition schemes. Srinivasan *et al.* have pointed out that the strengths of the self-generated magnetic field and the Hall parameter are estimated to be of the order of 10^2–10^3 T and in the range between 0.1 and 1, respectively, in National Ignition Facility implosions [33,34]. In such a strong self-generated magnetic field, anisotropic thermal conduction may affect hydrodynamic instability growth and thermal energy transports during hot-spot generation. The reported experimental platform is a unique test bed for studying MHD phenomena in laboratory astrophysics and laser fusion research. The anisotropic thermal transport is still a hypothesis to explain some of our experimental results based on the simulation. In future work, it will be necessary to measure directly the temperature and density of ablating plasmas in the external magnetic field to verify more details of the simulation code.

ACKNOWLEDGMENTS

The authors thank the technical support staff of ILE and the Cyber Media Center at Osaka University for assistance with the laser operation, target fabrication, plasma diagnostics, and computer simulations. The authors acknowledge Prof. Mima (GPI), Prof. Johzaki (HU), Dr. Sunahara (ILT), Dr. Santos and Prof. Batani (CELIA), and Dr. Logan (LLNL) for valuable discussions about this work. This work was supported through the Collaboration Research Programs by the National Institute for Fusion Science (Grants No. NIFS12KUGK057, No. NIFS11KUGK053, and No. NIFS15KUGK087) and by the Institute of Laser Engineering at Osaka University (Grants No. 2014A1-37, No. 2015A1-19, and No. 2016A1-FUJIOKA), through Grants-in-Aid (KAKENHI) for Young Scientists (Grant No. 24684044), for Challenging Research (Grant No. JP16K13918), and for Scientific Research (A) (Grant No. JP16H02245) by the Japanese Ministry of Education, Science, Sports, and Culture, and through the Bilateral Program for Supporting International Joint Research and a Grant-in-Aid for Fellows (Grant No. 14J06592) by the Japan Society for the Promotion of Science (JSPS).

[1] S. Masuda, T. Kosugi, H. Hara, S. Tsuneta, and Y. Ogawara, Nature **371**, 495 (1994).
[2] G. Valyavin, D. Shulyak, G. A. Wade, K. Antonyuk, S. V. Zharikov, G. A. Galazutdinov, S. Plachinda, S. Bagnulo, L. F. Machado, M. Alvarez *et al.*, Nature **515**, 88 (2014).
[3] H. Isobe, T. Miyagoshi, K. Shibata, and T. Yokoyama, Nature **434**, 478 (2005).
[4] R. Keppens, O. Porth, R. Monceau-Baroux, and S. Walg, Plasma Phys. Control. Fusion **55**, 124038 (2013).
[5] J. M. Stone and T. Gardiner, Phys. Fluids **19**, 094104 (2007).
[6] K. Chambers and L. K. Forbes, Phys. Plasmas **19**, 102111 (2012).
[7] D. Lecoanet, I. J. Parrish, and E. Quataert, Month. Not. R. Astron. Soc. **423**, 1866 (2012).
[8] T. Sano, T. Inoue, and K. Nishihara, Phys. Rev. Lett. **111**, 205001 (2013).
[9] D. S. Balsara, A. J. Bendinelli, D. A. Tilley, A. R. Massari, and J. C. Howk, Month. Not. R. Astron. Soc. **386**, 642 (2008).
[10] C. Plechaty, R. Presura, and A. A. Esaulov, Phys. Rev. Lett. **111**, 185002 (2013).
[11] B. Albertazzi, A. Ciardi, M. Nakatsutsumi, T. Vinci, J. Béard, R. Bonito, J. Billette, M. Borghesi, Z. Burkley, S. N. Chen *et al.*, Science **346**, 325 (2014).
[12] S. A. Slutz, M. C. Herrmann, R. A. Vesey, A. B. Sefkow, D. B. Sinars, D. C. Rovang, K. J. Peterson, and M. E. Cuneo, Phys. Plasmas **17**, 056303 (2010).
[13] P. Y. Chang, G. Fiksel, M. Hohenberger, J. P. Knauer, R. Betti, F. J. Marshall, D. D. Meyerhofer, F. H. Séguin, and R. D. Petrasso, Phys. Rev. Lett. **107**, 035006 (2011).
[14] D. J. Strozzi, M. Tabak, D. J. Larson, L. Divol, A. J. Kemp, C. Bellei, M. M. Marinak, and M. H. Key, Phys. Plasmas **19**, 072711 (2012).
[15] L. J. Perkins, B. G. Logan, G. B. Zimmerman, and C. J. Werner, Phys. Plasmas **20**, 072708 (2013).
[16] H. Nagatomo, T. Johzaki, A. Sunahara, H. Sakagami, K. Mima, H. Shiraga, and H. Azechi, Nucl. Fusion **53**, 063018 (2013).
[17] M. R. Gomez, S. A. Slutz, A. B. Sefkow, D. B. Sinars, K. D. Hahn, S. B. Hansen, E. C. Harding, P. F. Knapp, P. F. Schmit, C. A. Jennings *et al.*, Phys. Rev. Lett. **113**, 155003 (2014).
[18] W.-M. Wang, P. Gibbon, Z.-M. Sheng, and Y.-T. Li, Phys. Rev. Lett. **114**, 015001 (2015).

[19] H. Nagatomo, T. Johzaki, T. Asahina, A. Sunahara, T. Sano, H. Sakagami, K. Mima, S. Fujioka, H. Shiraga, and H. Azechi, Nucl. Fusion **55**, 093028 (2015).
[20] T. Johzaki, T. Taguchi, Y. Sentoku, A. Sunahara, H. Nagatomo, H. Sakagami, K. Mima, S. Fujioka, and H. Shiraga, Nucl. Fusion **55**, 053022 (2015).
[21] H. Daido, F. Miki, K. Mima, M. Fujita, K. Sawai, H. Fujita, Y. Kitagawa, S. Nakai, and C. Yamanaka, Phys. Rev. Lett. **56**, 846 (1986).
[22] C. Courtois, A. D. Ash, D. M. Chambers, R. A. D. Grundy, and N. C. Woolsey, J. Appl. Phys. **98**, 054913 (2005).
[23] S. Fujioka, Z. Zhang, K. Ishihara, K. Shigemori, Y. Hironaka, T. Johzaki, A. Sunahara, N. Yamamoto, H. Nakashima, T. Watanabe, H. Shiraga, H. Nishimura, and H. Azechi, Sci. Rep. **3**, 1170 (2013).
[24] K. F. F. Law, M. Bailly-Grandvaux, A. Morace, S. Sakata, K. Matsuo, S. Kojima, S. Lee, X. Vaisseau, Y. Arikawa, A. Yogo *et al.*, Appl. Phys. Lett. **108**, 091104 (2016).
[25] X. X. Pei, J. Y. Zhong, Y. Sakawa, Z. Zhang, K. Zhang, H. G. Wei, Y. T. Li, Y. F. Li, B. J. Zhu, T. Sano, Y. Hara, S. Kondo, S. Fujioka, G. Y. Liang, F. L. Wang, and G. Zhao, Phys. Plasmas **23**, 32125 (2016).
[26] J. J. Santos, M. Bailly-Grandvaux, L. Giuffrida, P. Forestier-Colleoni, S. Fujioka, Z. Zhang, P. Korneev, R. Bouillaud, S. Dorard, D. Batani *et al.*, New J. Phys. **17**, 083051 (2015).
[27] B. J. Zhu, Y. T. Li, D. W. Yuan, Y. F. Li, F. Li, G. Q. Liao, J. R. Zhao, J. Y. Zhong, F. B. Xue, S. K. He *et al.*, Appl. Phys. Lett. **107**, 261903 (2015).
[28] L. Gao, H. Ji, G. Fiksel, W. Fox, M. Evans, and N. Alfonso, Phys. Plasmas **23**, 43106 (2016).
[29] E. T. Everson, P. Pribyl, C. G. Constantin, A. Zylstra, D. Schaeffer, N. L. Kugland, and C. Niemann, Rev. Sci. Instrum. **80**, 113505 (2009).
[30] http://www.esrf.eu/Accelerators/Groups/InsertionDevices/Software/Radia/Documentation/Introduction.
[31] Y. T. Li, Y. Zhang, S. J. Wang, X. Liu, Q. L. Dong, J. Y. Zhong, F. L. Wang, J. R. Shi, G. Zhao, J. Y. Zhang *et al.*, *Opt. InfoBase Conf. Pap.* (IEEE, New York, 2009), pp. 1–2.
[32] M. J.-E. Manuel, C. K. Li, F. H. Séguin, J. Frenje, D. T. Casey, R. D. Petrasso, S. X. Hu, R. Betti, J. D. Hager, D. D. Meyerhofer *et al.*, Phys. Rev. Lett. **108**, 255006 (2012).
[33] B. Srinivasan, G. Dimonte, and X.-Z. Tang, Phys. Rev. Lett. **108**, 165002 (2012).
[34] B. Srinivasan and X. Z. Tang, Phys. Plasmas **19**, 082703 (2012).
[35] A. Nishiguchi, T. Yabe, M. G. Haines, M. Psimopoulos, and H. Takewaki, Phys. Rev. Lett. **53**, 262 (1984).
[36] T. Sakaiya, H. Azechi, M. Matsuoka, N. Izumi, M. Nakai, K. Shigemori, H. Shiraga, A. Sunahara, H. Takabe, and T. Yamanaka, Phys. Rev. Lett. **88**, 145003 (2002).
[37] H. Azechi, T. Sakaiya, S. Fujioka, Y. Tamari, K. Otani, K. Shigemori, M. Nakai, H. Shiraga, N. Miyanaga, and K. Mima, Phys. Rev. Lett. **98**, 045002 (2007).
[38] S. G. Glendinning, S. N. Dixit, B. A. Hammel, D. H. Kalantar, M. H. Key, J. D. Kilkenny, J. P. Knauer, D. M. Pennington, B. A. Remington, R. J. Wallace *et al.*, Phys. Rev. Lett. **78**, 3318 (1997).
[39] V. A. Smalyuk, S. X. Hu, V. N. Goncharov, D. D. Meyerhofer, T. C. Sangster, C. Stoeckl, and B. Yaakobi, Phys. Plasmas **15**, 082703 (2008).
[40] V. A. Smalyuk, S. X. Hu, V. N. Goncharov, D. D. Meyerhofer, T. C. Sangster, D. Shvarts, C. Stoeckl, B. Yaakobi, J. A. Frenje, and R. D. Petrasso, Phys. Rev. Lett. **101**, 025002 (2008).